# Effect of linear defects on the field distribution in thin superconductors

Mahesh Chandran
*Low Temperature Physics Group, Centre for Advanced Technology, Indore, India 452013*
(Received 27 May 1997; revised manuscript received 28 August 1997)

A two-dimensional Josephson-junction array with linear defects is simulated to probe the influence of twin boundaries on the magnetic-field distribution in a thin superconductor in a transverse magnetic field. The simulation was carried out for varying pinning potentials $\alpha$ of the defect, and for different orientations $\theta_d$ of the defect relative to the external boundary. For $\alpha<1$ (weak pinning), the defect behaves as an easy channel for longitudinal motion of the vortices, whereas transverse motion across the defect is hindered due to vortices within the defect channel. For intermediate angle $\theta_d$, a gliding motion outside the fore-edge (edge facing the interior of the array) of the defect is observed. For $\alpha>1$, the defect acts as a barrier for transverse as well as longitudinal motion of the vortices, resulting in an increased vortex density in the wake of the defect for intermediate values of $\theta_d$. [S0163-1829(98)00606-7]

The effect of correlated disorder on the bulk pinning of the vortex lattice has received much attention with the discovery of high-$T_c$ superconductors. Of particular importance is the role of twin boundaries (TB's) which are formed naturally during the growth process and are characterized by spatial correlation extending over a macroscopic length scale. The magnetization[1] and transport properties[2] of twinned and detwinned crystals have unambiguously shown that TB's determine the behavior of the vortex lattice over a wide region of the $H$-$T$ phase diagram. Bitter decoration of vortices[3] has shown vortex strings commensurate with the TB's giving direct evidence for vortex pinning by extended disorders. Using the magneto-optical method which allows spatiotemporal imaging of the vortex dynamics, Duran *et al.*[4] showed that for longitudinal motion of vortices, the TB's act as channels for easy flow, whereas the transverse motion across the TB is hindered (barrier nature). On the other hand, experiments by Vlasko-Vlasov *et al.*[5] observed that TB's act solely as a planar barrier which causes vortices to pile up close to the defect edge facing the incoming flux front. This was interpreted as evidence for the guided motion of vortices by the TB's. Subsequent experiments[6] resolved the contradiction by noting that the two experiments probed different regimes (easy-flow channel and barrier nature) of the pinning behavior of the TB's. One pertinent question raised by these experiments was whether flux motion occurs inside the twin region or just outside of it (guided motion) which could not be resolved due to limited resolution of the magneto-optical methods. Pinning by TB's is also observed to be sensitive to the pinning of the vortex lattice in the untwinned region.[7]

Vortex dynamics in the presence of TB's have been simulated numerically for the infinite slab geometry (demagnetization factor $N=0$). Crabtree *et al.*[8] found guided motion of the vortices external to the TB for small transport current. Groth *et al.*[9] observed that the barrier behavior crosses over to channel behavior with varying angle $\theta_d$ between the TB and the driving force, and the ratio between the threshold force in the twinned and the untwinned region. In the slab geometry, the relation between the field and the screening current is local, whereas the experiments are carried out generally on thin superconductors in the transverse magnetic field ($N\rightarrow 1$) for which the vortex field and current are related *nonlocally*. This leads to nonuniform field distribution in finite-size rectangular superconductors with little penetration of the field around corners. Also, the interaction of the TB's with the vortices becomes nontrivial, depending critically on the orientation of the TB relative to the penetrating flux front.

Field distribution in a thin superconductor in a transverse magnetic field is explained within the critical state model.[10] For an arbitrary shaped boundary, a formalism has been developed[11] wherein the field distribution is obtained as solution to the nonlinear diffusion equation for the field with a phenomenological relation between the electric field **E** and the current density **J**. In recent years, the two-dimensional (2D) Josephson-junction array (JJA) with screening effect have been studied extensively in the context of vortex dynamics.[12] The screening effect is included via the geometrical inductance matrix of the array.[13] The induced current drives the vortices towards the interior of the array. On the other hand, discreteness of the array provides a pinning potential to the vortices at the plaquette center.[14,13] These two competing forces lead to an equilibrium field distribution similar to that predicted by the critical state model for a thin superconductor in a transverse magnetic field.[15] It is essential to emphasize here that the simulation uses only the Josephson relation and does *not* involve any *a priori* assumption regarding the field and current relation. Here, we investigate the effect of the extended defect on the equilibrium field distribution, and thus simulate the behavior of TB in thin superconductors in a transverse magnetic field. The calculation is carried out for different orientations $\theta_d$ of the line defect with respect to the external boundary. On the other hand, the ratio of the critical current in the defect region to that in the undefected region $\alpha=I_{c,\mathrm{def}}/I_c$ is varied to simulate the effect of the varying pinning potential of the defect channel. Also, the effect on the field distribution due to interaction between defects is considered.

We consider an array of $N_x\times N_y$ square plaquettes forming a homogeneous network of Josephson junctions in the $x$-$y$ plane. The junction dynamics is governed by the time evolution of the gauge-invariant phase difference across it.

 

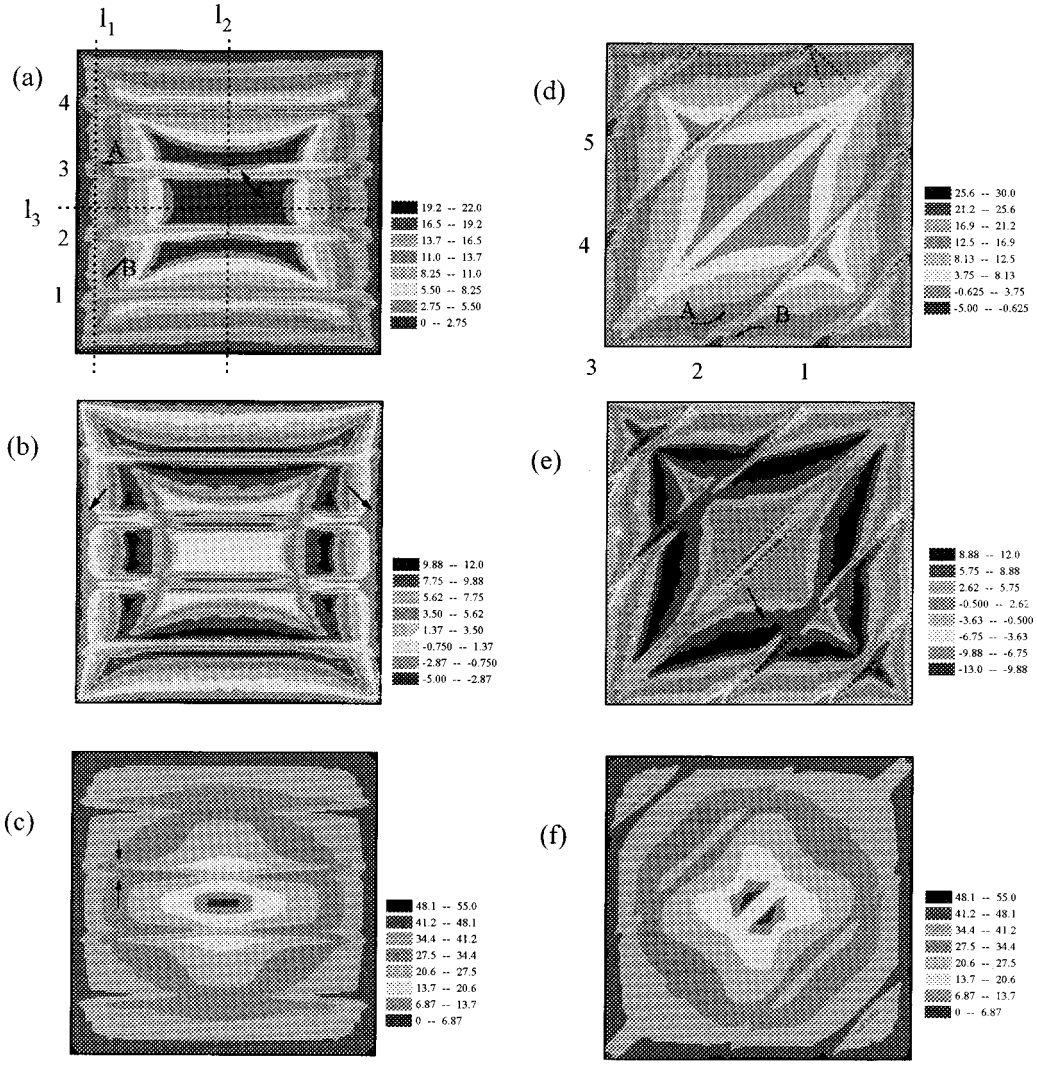


FIG. 1. The density plot of the field distribution in a square array with line defects along the [10] direction for (a) $f=15$, (b) remanence of (a), (c) $f=40$. The field distribution for defects along the [11] axis is shown for (d) $f=20$, (e) remanence of (d), (f) $f=40$. The details are explained in the text.

This is modeled using the resistively-shunted junction equation[16] appropriate for the overdamped junctions

$$\frac{\Phi_0}{2\pi R}\frac{d\phi}{dt}+I_c\sin\phi=I_b, \tag{1}$$

where the variables $\phi$ and $I_b$ are the gauge-invariant phase difference and the current across the junction, respectively, written as column vectors. The resistance and the critical current of the junction is represented by $R$ and $I_c$, respectively, and $\Phi_0(=hc/2e)$ represents a quantum of flux. The flux $\Phi$ in the plaquette is given by the directed sum of gauge-invariant phase differences around the plaquette (taken in the anticlockwise sense) which is conveniently written as

$$\mathsf{M}\phi=2\pi\frac{\Phi}{\Phi_0}=-2\pi f-\frac{1}{\lambda}LI_m, \tag{2}$$

where $\mathsf{M}$ is the loop-sum-operator matrix[13] and $L$ is the geometrical inductance matrix of the array. The current in the plaquette is represented by the column vector $I_m$, whereas the applied flux is denoted by $f=\Phi_{\rm ext}/\Phi_0$. Also, $\lambda=\Phi_0/2\pi L_0 I_c$ where $L_0$ is the self-inductance of the plaquette. $\sqrt{\lambda}$ defines the dimensionless penetration depth similar to London's penetration depth for a bulk superconductor. For the JJA with full inductance matrix, the effective penetration depth is given as $\lambda_\perp=\lambda/(\mu_0 p/L_0)>\lambda$, where $p$ is the lattice constant of the array, analogous to the enhanced $\lambda$ for a thin superconductor in a transverse magnetic field. The elements of the mutual inductance matrix are dependent on the geometry of the superconducting island and are calculated for the + shape which is approximated by rectangular bars of length $p$ and width $0.45p$. Note that only the functional dependence $L(\mathbf{r},\mathbf{r}')=L(|\mathbf{r}-\mathbf{r}'|)$ finally enters the simulation which for the 2D geometry is observed to be of the form $L(\mathbf{r},\mathbf{r}')\sim 1/|\mathbf{r}-\mathbf{r}'|^3$ for distances beyond four or five lattice constants.

The junction current in Eq. (1) can be written in terms of plaquette current, $\mathsf{M}^T I_m=I_b$, where $\mathsf{M}^T$ denotes the transpose of $\mathsf{M}$. Introducing the dimensionless time $\tau[=(2\pi R I_c/\Phi_0)t]$, the equation of motion for the array can be rewritten as

$$\frac{d\phi}{d\tau} = \mathsf{M}^T \tilde{I}_m - \alpha \sin\phi,$$

$$\mathsf{M}\phi = -2\pi f - \frac{\alpha}{\lambda}\tilde{L}\tilde{I}_m, \tag{3}$$

where, $\tilde{L} = L/L_0$ and $\tilde{I}_m = I_m/I_c$ are the reduced inductance matrix and plaquette currents, respectively. The defect is introduced through the parameter $\alpha = I_{c,\mathrm{def}}/I_c$, where $I_{c,\mathrm{def}}$ is the critical current of junctions in the defect region. As has been shown before,[13,14] the pinning potential experienced by a vortex at the center of the plaquette is proportional to the junction current. Thus, by varying $\alpha$, the pinning potential of the defect can be changed relative to the undefected region. Along the defect, the critical current is assumed to be constant. Free-end boundary conditions are used to simulate the experimental situation. The above equations are solved using the variable-step Runge-Kutta method and fast-Fourier-transform accelerated-matrix multiplication,[13] the details of which are given in Ref. 17. Generally, the equations are iterated for nearly $1400\tau$ of which the first $600\tau$ iterations are neglected to avoid transients. The remaining iterations are performed to obtain the time-averaged flux $\Phi(n_x, n_y)$ in the array.

The simulations were performed for square ($N_x = N_y = 64$) and rectangular ($N_x = 64, N_y = 32$) arrays for $\lambda = 0.01$. As has been observed before,[15] for any applied field, the magnetization of the array saturates for $\lambda \leqslant 0.01$, implying a strong screening regime. For this regime, the field distribution is observed to be similar to the field distribution obtained within the critical state theory for a thin continuum superconductor. For a continuum superconductor, the above choice of $\lambda$ sets the length scale $p = \lambda_L^2/\lambda d$, where $\lambda_L$ is the London penetration depth and $d$ is the thickness. For high-$T_c$ superconductors, where $\lambda_L$ is typically of the order $10^3 - 10^4$ Å, for a sample of thickness of $1 - 10$ $\mu$m, $p \approx 10 - 100\lambda_L$. This sets a lower limit to the length scale of the field distribution presented here. The field distribution for the homogeneous array shows that for $f_p \approx 25$, the array is fully penetrated by the magnetic flux (the actual magnetic field in experiments can be obtained as $f/f_p$, as $f_p$ is dependent on the exact geometry of the sample). From the magnetization, an effective demagnetization factor $N \approx 0.95$ is obtained, indicating the 2D magnetic response of the array. The defect is chosen to be 2 or 3 plaquettes wide.

Figures 1(a)–1(c) shows the two-dimensional density plot of the field distribution in the array with defects oriented along the [10] direction [marked D1–D4 in Fig. 1(a)] for $\alpha = 0.05$. The plots are for $f = 15 (< f_p)$, and for $f = 40$ $(> f_p)$. The remanent field distribution is shown for $f = 15$. Maximum field penetration can be seen to occur through the middle of the external boundaries, forming a convex flux front in the undefected region as expected from the conventional critical state model.[11] Around the corners where the screening current bends sharply, the flux penetration is minimum.

The complete field penetration of defects for $f < f_p$ indicates that defects are easy-flow channels for the magnetic flux [note that in Fig. 1(a), the central undefected region is in the shielded state, i.e., $\mathbf{B} = 0$, though field has penetrated into the array along D2 and D3]. Along the defect channel D1, the field distribution is uniform whereas it shows nonmonotonic variation along D2, as shown in the one-dimensional plot in Fig. 2(a). The nonmonotonic field distribution along the defect occurs for $f < f_p$ and vanishes for large $f > f_p$ as can be seen from Fig. 2(c). This can be understood as arising due to the convexity of the flux front for partial penetration of the array. The transverse behavior of defects differs substantially along line $l_1$ and $l_2$ [see Fig. 1(a)]. Along $l_2$, $\Phi(n_y)$ shows a sharp peak at the fore-edge of the defect (edge facing the interior of the array), whereas close to the hind-edge (edge facing the external boundary) a low-field region is observed implying a barrier nature of the defect for transverse motion of the magnetic flux. Note that barrier nature need not imply accumulation of vortices along the defect edge.[9] On the contrary, one expects lowering of the vortex density due to repulsion by the vortices within the channel due to easy flow along the longitudinal direction. This explains the decrease in $\Phi$ in Fig. 2 outside D1 and D4 (marked by the arrows). In Fig. 1(a), one notices that near the external boundaries, the magnetic flux accumulates just outside D2 and D3 (marked B) with $\Phi$ decreasing in the defect region (marked A), as evident from the one-dimensional plot along $l_1$. This is contrary to the intuition as one expects larger field penetration along the defect region than compared to that in the undefected region. This also arises due to the convexity of the flux front for $f < f_p$. Thus, one observes a complicated behavior of the defects for small applied field $f < f_p$, depending strongly on its coordinates relative to the corner.

The remanent field distribution for $f = 15$ [Figs. 1(b) and 2(b)] shows that a substantial field is trapped along D2 and D3 in the central region of the array, whereas D1 and D4 act as an exit channel for the magnetic flux. Close to the external

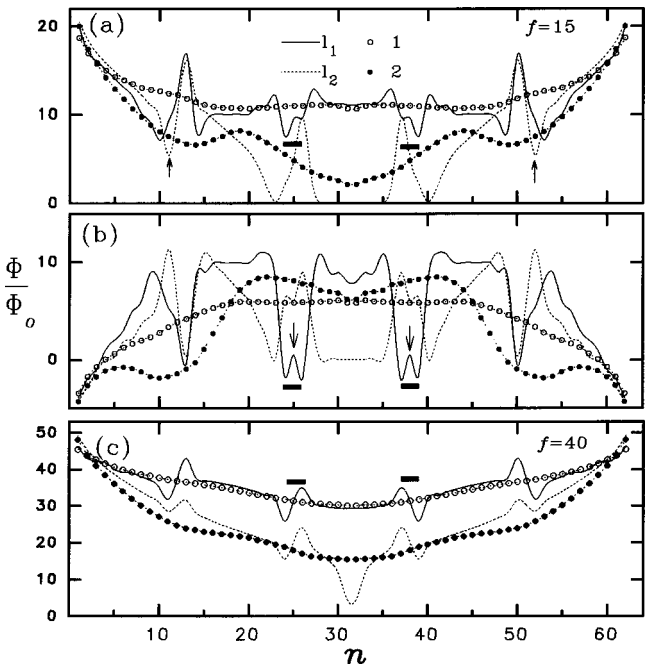


FIG. 2. The one-dimensional plot of the field distribution along the line $l_1$ and $l_2$, and along D1 and D2 in Fig. 1(a) for defects along the [10] axis. The defect position is shown by a thick dash.

boundary, one observes entry of antivortices into the array along D2 and D3 [marked by arrows in Fig. 2(b)] due to wrapping of the field lines around the array. This is a *nonlocal* effect and clearly shows that the array indeed simulates the electromagnetic behavior of a thin superconductor in the transverse magnetic field. The one-dimensional plot along $l_2$ shows that the defect acts as a barrier for transverse motion, thus inhibiting the exit of the magnetic flux.

For $f=40>f_p$, the effect due to the convex flux-front vanishes [see Fig. 2(c)]. Large penetration by the magnetic flux outside the defect gives a characteristic ''flame''-shaped field distribution [Fig. 1(c)] similar to that observed experimentally.[18] The origin of the flame-shaped distribution [marked in Fig. 1(c)] at high field can be understood as arising due to increased flux density in the defect channel which gives rise to a transverse component to the flux motion close to the external boundary of the array. This implies that the flame-shaped field distribution should be observable beyond a certain vortex density in the defect channel. The one-dimensional plot for $f=40$ [Fig. 2(c)] shows that the longitudinal and transverse field distribution is similar for all the defects [note that the peak position in Fig. 2(c) coincides for $l_1$ and $l_2$].

For defects oriented along the [11] direction, the vortex dynamics is altered remarkably. Figures 1(d)–1(f) shows the field distribution for the same value of $\alpha$ as that for defects along the [10] direction. The plots are for the externally applied field $f=20$ [Fig. 1(d)] and $f=40$ [Fig. 1(f)], and for the remanent state of $f=20$ [Fig. 1(e)]. The magnetic field penetrates to the center of the array through the defect along the diagonal [D3 in Fig. 1(d)]. Interestingly, in the undefected square array, the vortex motion along the diagonal does not occur due to bending of the current streamlines along it (this is also observed in the continuum superconductor[19]). The striking feature is the observation of field distribution due to an apparent gliding of vortices outside the fore edge [region marked A in Fig. 1(d)]. The gliding of vortices along the fore edge occurs in response to a field gradient set across the edge due to increased flux *within* the defect channel. Note that this mechanism is different from the observation of Ref. 5 where gliding motion occurs along the wake of the defect (hind edge) due to the barrier nature of the TB. The results are in agreement with the simulation of TB in the presence of a small external current by Crabtree *et al.*[8] A low-field region is observed close to the hind edge [marked region B in Fig. 1(d)] near the external boundary. This can be explained as due to enhanced flux density inside the defect leading to an enhanced vortex-vortex interaction. A remarkable feature is the nucleation of antivortices along the hind edge for small applied fields and the weak pinning potential of the defect channel (this is more evident in Fig. 3, see below). This is solely due to the large demagnetization effect in a 2D geometry which leads to a turning around of the field lines of the magnetic flux accumulated close to the fore edge (region A). But note that nucleation of antivortices is possible only due to creation of the low-field region close to the hind edge (see below). The bending of streamlines close to the defect gives rise to characteristic lines in region A, marked as C in Fig. 1(d). In the remanent state, the fore edge projects an acute angle to the direction of motion of the magnetic flux (directed towards the external boundary). Thus, the defect acts as a barrier trapping the field in region A [marked by the arrow in Fig. 1(e)]. In large applied fields [$f=40$, Fig. 1(f)], the field penetration is complete along all defects.

The pinning behavior of the TB has been observed to vary with changing bulk pinning of the vortex lattice in the untwinned region. At low temperatures, the vortex pinning in the untwinned region is strong (large $J_c$), and the small driving force sets the vortices into motion along the TB (channel behavior). With increasing temperature, increased thermal fluctuation in 3D leads to exponential decrease of the critical current density in the untwinned region. On the other hand, translational invariance along the TB reduces the dimension of the thermal fluctuation,[20] giving a slow algebraic decrease of the critical current density in the twinned region. Thus, at high temperatures, the TB's become effective centers for vortex pinning. To simulate this crossover, we note that $\alpha$ parametrizes the pinning potential of the linear defect in the array, which can be varied relative to the undefected region. Figures 3(a)–3(d) show the field distribution in the array with defects oriented along the [11] direction for $f=15$ with increasing $\alpha$. For $\alpha=0.005$ [Fig. 3(a)], the magnetic flux penetrates into the array along the defect channel and by gliding outside the fore edge of the defect. The presence of antivortices close to the hind edge is shown by the arrows. For $\alpha=0.2$ [Fig. 3(b)], the defect channel is penetrated partially and one observes a central shielded region (the antivortices can still be observed). For $\alpha=0.6$ [Fig. 3(c)], the shielded fraction of the array increases, indicating increased bulk pinning of the magnetic flux. Field penetration due to the gliding motion of vortices is reduced, consequently increasing the flux density along the wake of the defect, which can be seen from the one-dimensional plot [Fig. 3(e), upper frame] along the dotted line in Fig. 3(a). This causes the antivortices to disappear and corroborates the view that its origin lies in the formation of the low-field region around the wake of the defects coupled with the large demagnetization factor (see the previous para). For $\alpha=1.2$, the defect behavior changes drastically. The defect becomes a strong barrier for the transverse motion of the magnetic flux resulting in accumulation of magnetic flux in the wake of the defects [marked by the arrows in Fig. 3(d)]. An apparent gliding of the flux can also be seen along the hind edge, in contrast to the case of $\alpha<1$ for which it occurs along the fore edge. This is consistent with the experimental observation of Ref. 5 which was done at high temperatures. Thus, the simulation unambiguously shows that the behavior of TB's is dependent strongly on the pinning of the vortex lattice in the untwinned region, and can be tuned by varying the temperature.

The field distribution is strongly influenced by the orientation of the defect $\theta_d$ with respect to the external boundary. Figure 4(a) shows the field distribution for $f=15$ with increasing angle $\theta_d$ of a single defect in a rectangular array for $\alpha=0.05$. For decreasing $\theta_d$, the field penetration due to gliding of vortices along the defect edge increases (note the region marked by the arrows). The magnetic-field penetration along the defect, $l_{\mathrm{def}}=l_{\mathrm{def}}(\alpha,\theta,f)$, is maximum for the intermediate angle for $f<f_p$. For a thin superconductor, the nonlocal relation between the currents and the field can lead to a strong interaction between the TB's. Figures 4(b)–4(c) show the field distribution in the rectangular array with varying

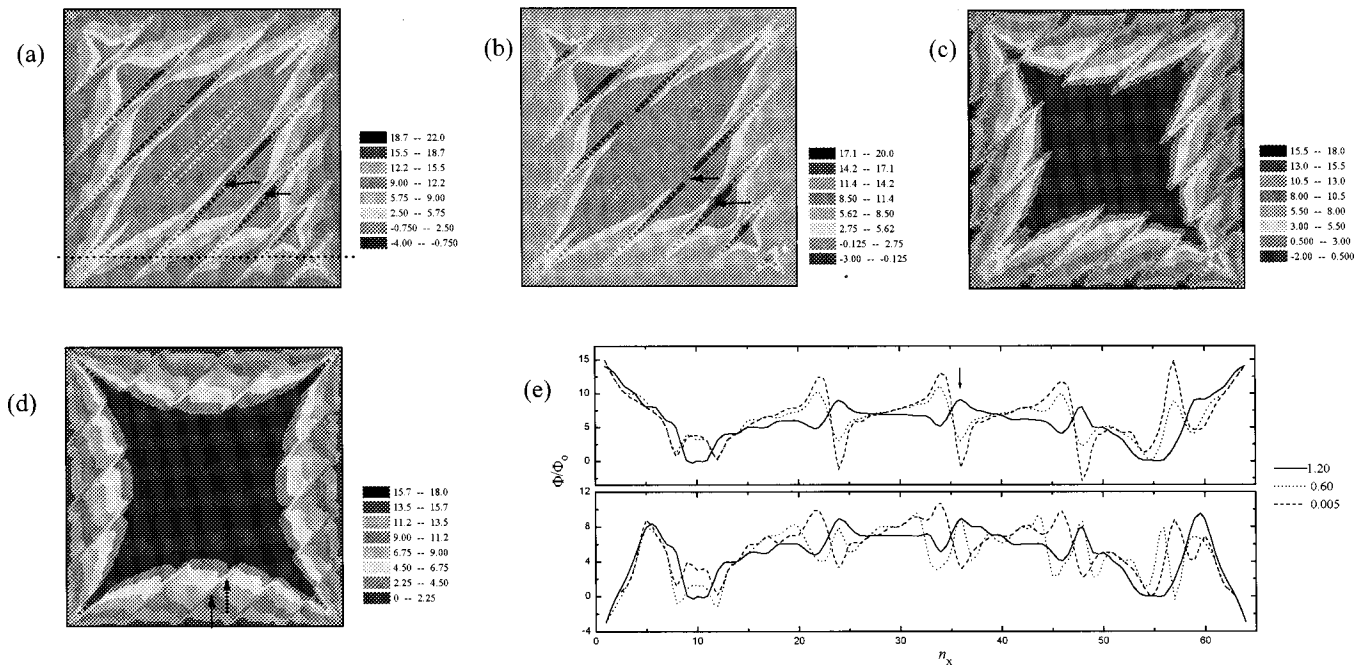


FIG. 3. The field distribution in the array ($f=15$) with defects along the [11] axis for increasing $\alpha$ (a) 0.005, (b) 0.2, (c) 0.6, and (d) 1.2. The one-dimensional plot along the dotted line in (a) is shown in the upper frame of (e), with the lower frame showing the remanence field distribution. Note the shift in peak for $\alpha=1.2$ as shown by the arrow in (e), indicating a pile up of vortices in the wake of the defect. Nucleation of antivortices is shown by the arrows in (a) and (b).

separation between two linear defects [marked 1 and 2 in Fig. 4(b)] for $f=20$ and $\alpha=0.05$. One observes larger vortex penetration along defect 1 as compared to the field penetration along defect 2. This can be understood as arising due to increased flux density in defect 1 which interacts repulsively with the vortices within defect 2. For large separation, the defects acts as an independent channel for the magnetic flux. The interaction between the defects can be quantified by defining a length scale $l_h=l_h(\alpha,\theta,f)$ over which the effect of a single defect is ''healed'' inside the undefected region. For defect separation less than $l_h$, the interaction is expected to be strong.

In summary, the field distribution in the Josephson-junction array with linear defects is presented and compared

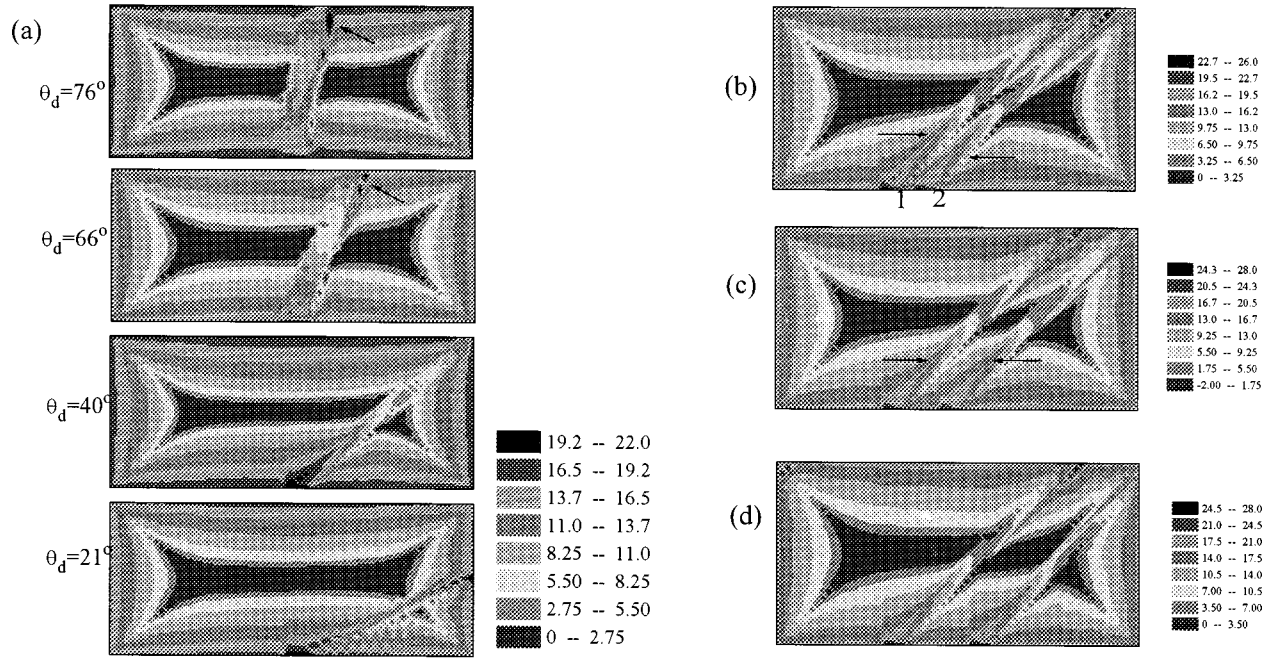


FIG. 4. (a) The field distribution with varying angle $\theta_d$ of a single defect in a rectangular array for $f=10$ and $\alpha=0.05$. For intermediate angle $\theta_d$, the gliding motion of the vortices outside the defect is a prominent feature. The field distribution for two linear defects separated by a distance (b) $2p$, (c) $6p$, and (d) $10p$ for $f=20$ and $\alpha=0.05$.

with the behavior of twin boundaries in thin superconductors. The defect behavior changes from that of the easy-flow channel to that of a barrier with increasing pinning potential of the defect. This is in excellent agreement with the experimental observations of Refs. 4 and 5. The vortex penetration along the defect channel is maximum for the defect inclined at an intermediate angle with respect to the external boundary. Also, the nonlocal effects in a 2D geometry can lead to interaction between TB's.

The author is grateful to Dr. P. Chaddah for critical reading of the manuscript. Also, the author acknowledges the Computer Center, CAT, for the prolonged use of the computational facility, and CSIR (India) for the financial assistance.

[1] M. Oussena *et al.*, Phys. Rev. B **51**, 1389 (1995); A. A. Zhukov *et al.*, *ibid.* **52**, 9871 (1995); E. M. Gyorgy *et al.*, Appl. Phys. Lett. **56**, 2465 (1990).
[2] W. K. Kwok *et al.*, Phys. Rev. Lett. **76**, 4596 (1996); Steven Fleshler *et al.*, Phys. Rev. B **47**, 14 448 (1993); H. Safar *et al.*, Appl. Phys. Lett. **68**, 1853 (1996).
[3] G. J. Dolan *et al.*, Phys. Rev. Lett. **62**, 827 (1989).
[4] C. A. Durán *et al.*, Nature (London) **357**, 474 (1992).
[5] V. K. Vlasko-Vlasov *et al.*, Phys. Rev. Lett. **72**, 3246 (1994).
[6] C. A. Durán *et al.*, Phys. Rev. Lett. **74**, 3712 (1995); U. Welp *et al.*, *ibid.* **74**, 3713 (1995).
[7] Zhukov *et al.*, Phys. Rev. B **52**, R9871 (1995).
[8] G. W. Crabtree *et al.*, Physica C **263**, 401 (1996).
[9] J. Groth *et al.*, Phys. Rev. Lett. **77**, 3625 (1996).
[10] E. H. Brandt, Rep. Prog. Phys. **58**, 1465 (1995).
[11] E. H. Brandt, Phys. Rev. Lett. **74**, 3025 (1995); Phys. Rev. B **52**, 15 442 (1995).
[12] T. Wolf *et al.*, Phys. Rev. B **47**, 5383 (1993); D. Dominguez *et al.*, *ibid.* **53**, 11 692 (1996); Mahesh Chandran *et al.*, Physica C **267**, 59 (1996); D. Reinel *et al.*, *ibid.* **245**, 193 (1995).
[13] J. R. Phillips *et al.*, Phys. Rev. B **47**, 5219 (1993).
[14] C. J. Lobb *et al.*, Phys. Rev. B **27**, 150 (1983).
[15] Mahesh Chandran, Physica C **289**, 22 (1997).
[16] A. Barone and G. Paterno, *Physics and Application of Josephson Effect* (Wiley, New York, 1982).
[17] Mahesh Chandran, Phys. Rev. B **56**, 6169 (1997).
[18] U. Welp *et al.*, Physica C **235**, 241 (1994).
[19] Th. Schuster *et al.*, Phys. Rev. B **52**, 10 375 (1995).
[20] G. Blatter *et al.*, Rev. Mod. Phys. **66**, 1125 (1994).